Acta Crystallographica Section A
Foundations of Crystallography
ISSN 0108-7673

Received 12 February 2008
Accepted 10 October 2008

Two-wavelength inversion of multiply scattered soft X-ray intensities to charge density

J. C. H. Spence

Department of Physics, Arizona State University, Tempe, AZ 85287-1504, USA. Correspondence e-mail: spence@asu.edu

A method is described for reconstructing the two-dimensional real-space charge density of an isolated object from measurement of the soft X-ray transmission diffraction pattern when it is affected by strong multiple scattering. The Bloch-wave scattering-matrix approach is used to show that the diffracted amplitude depends only on a simple product of X-ray wavelength and sample thickness (unlike the case of relativistic electron diffraction) under reasonable approximations. The multislice formulation then gives the effect of a small change in wavelength, which involves only single scattering. Dynamical diffraction patterns are recorded at two adjacent wavelengths, phased by iterative methods, transformed to real space and divided to give a single-scattering wavefunction. This can then be used to produce a charge-density map. The extension of the method to tomography is discussed. Consideration is first also given to the possibility that absorption due to the photoelectric effect may be so severe for soft X-rays that multiple elastic scattering becomes so much less probable than photoelectric absorption that it may be neglected entirely. A discussion of signs in soft X-ray, positron and electron multiple-scattering theory is given.

1. Introduction

The strength of multiple elastic scattering, which prevents a straightforward inversion of diffraction patterns to real-space images (even beyond the phase problem), is characterized by several parameters which take on differing values for hard X-ray, soft X-ray, electron, positron and neutron diffraction. For two-dimensional soft X-ray and electron diffraction in the projection approximation, the reconstruction of the sample charge density (or potential) may be understood to be a two-step process, in which the phase problem is solved for the far-field diffracted intensities, and the two-dimensional Fourier transform of these provides the complex 'exit-face wavefunction'. This is only simply related to the projected charge density (or potential) under conditions of single scattering; otherwise a real-space map of the charge density (potential) cannot be obtained. (For three-dimensional hard X-ray diffraction from small-unit-cell crystals, neither the projection approximation nor the exit-face wavefunction are used, but similar difficulties arise.) The parameters that define the validity domain of the single-scattering approximation include the beam-energy-dependent strength of the elastic interaction (often characterized by an extinction distance) and, in the transmission geometry, the sample thickness. Equally important are absorptive (inelastic) effects such as the photoelectric effect for X-ray diffraction, which may provide an effective limit on thickness, and hence on the severity of multiple scattering. If diffraction is described using an optical potential and a suitable wave equation, the real and imaginary parts of this potential [or complex refractive index $n = (1 - \delta) - i\beta$] provide a fixed, sample-dependent quantity whose relative contributions to elastic and inelastic scattering can be varied only by the choice of beam energy. In this paper we consider only hydrated protein samples, for which this ratio of elastic to inelastic cross sections is a well known function of beam energy. It then controls the amount of information that can be extracted from the ground state by elastic scattering per unit damage by inelastic scattering. We compare the soft X-ray and high-energy electron diffraction single-scattering regimes, and consider the possibility that absorption effects may be so severe for a soft X-ray beam energy near an inner-shell absorption edge that photoelectron production becomes much more probable than a second elastic scattering event. In that favorable case, multiple scattering might be neglected altogether. We then discuss the inversion of multiply scattered intensities to give the sample charge density, and describe successful simulations of inversion based on patterns recorded at two different beam energies.

The interaction Hamiltonian for both X-ray and electron diffraction separates into diagonal terms which derive from the kinetic energy of the beam and off-diagonal terms which depend on the potential energy or charge density. The diagonal geometric factors define the scattering kinematics and are related to the Fresnel number, the excitation error and the curvature of the Ewald sphere. Diffraction data are collected on this sphere, which imposes energy and momentum

conservation. As in band theory for electronic structure, this separation provides important insights into the nature of multiple scattering and the related problem of tomographic reconstruction. For the case where backscattering and polarization effects are negligible (as for soft X-ray diffraction), there have been at least five independent formulations of the multiple-scattering problem, following the early work of Ewald, Laue and Darwin on few-beam solutions [see James (1965) for a review]. For electron diffraction, these are the Bloch-wave solutions of Bethe (1929), the multislice approach [see Cowley (1995) for a review], the scattering-matrix approach (Sturkey, 1962), the Born series (Moody, 1972) and the coupled differential equations of Hirsch *et al.* (1977). For X-rays, Pinsker (1978) provides an excellent review. These are more-or-less independent theoretical formulations, leading to distinct algorithms which may be extended to nonperiodic samples by straightforward computational superlattice methods. Several researchers have demonstrated their equivalence in the many-beam case. Here we focus on the soft X-ray case, for which the essential single-scattering theory has been reviewed recently by Kirz *et al.* (1995).

Using new iterative solutions to the phase problem, three-dimensional images of nonperiodic objects have recently been reconstructed from their soft X-ray single-scattering diffraction patterns (Miao *et al.*, 1999; Chapman *et al.*, 2006; Shapiro *et al.*, 2005). The presence of multiple scattering, which destroys the simple Fourier-transform relationship of the first Born approximation between the scattered amplitudes and the sample charge density, has always been considered a severe limitation to this diffractive (or 'lensless') imaging technique (Thibault *et al.*, 2006). However, it has frequently been pointed out (Moody, 1968) that in a sense multiple scattering solves the phase problem, since, in crystals, it allows interference between different Bragg beams, making them sensitive to structure-factor phases. An approach to inversion with multiple scattering that takes advantage of this effect, based on projection between constrained sets in the manner of the hybrid input–output (HiO) algorithm, was described by Spence *et al.* (1999). A dynamical ptychography approach has also been described (Spence, 1998). All this contrasts with the single-scattering case, where additional numerical direct or other methods such as anomalous diffraction (MAD) or isomorphous replacement (SIR) must be used to extract phase information from crystal diffraction patterns.

Here we describe a scheme that allows direct inversion of soft X-ray diffraction patterns affected by strong multiple scattering to the two-dimensional sample charge density. We assume a nonperiodic object, whose continuous distribution of far-field scattering has been phased by the above iterative methods. This initial treatment is limited to the case where the sample charge density is not a function of the coordinate z taken along the beam. This solution to the phase problem provides the complex dynamical exit-face wavefunction (or equivalently, the complex multiply scattered far-field diffracted amplitudes), which bears no simple relationship to the sample charge density, but is used as the input to the inversion process. At least four such phasing methods have been demonstrated recently (HiO, in-line Gabor holography, ptychography and Fourier-transform holography), as reviewed elsewhere (Spence, 2007). These have had varying degrees of success in dealing with the 'complex object' (the exit-face wavefield) used here.

We first use Sturkey's scattering-matrix method to show that the multiple-scattering theory involves only simple products of wavelength and thickness, so that small changes in each are equivalent. Differentiation of the scattering matrix with respect to wavelength therefore provides the required single-scattering amplitudes if the charge density is not a function of the z coordinate along the beam direction. The approach here is similar to that described by Allen *et al.* (2001) for electron-microscope imaging of thin crystals using two thicknesses. In that method, because images formed by lenses are used, the resolution and aberrations of the image-forming lenses limit resolution, and their two-thickness method is applied to periodic objects. (The difficulties with two-wavelength electron-diffraction methods are discussed below.)

For soft X-rays, the neglect of both polarization and backscattering effects requires justification if the multislice method is to be used for simulation. The multiple scattering (and backscattering) of polarized hard X-rays by the aligned molecules of a crystal has been extensively studied and described by a Bloch-wavevector theory (*e.g.* Pinsker, 1978). This has been the basis of both X-ray standing-wave fluorescence experiments and accurate structure-factor measurements based on *Pendellösung* oscillations of Bragg intensities with thickness. The solution of coupled differential equations, one set for each polarization component, is then required for the complex amplitudes. For unpolarized or polarized soft X-rays incident on the unaligned molecules of an isolated nonperiodic sample (such as a biological cell) in the transmission geometry, a scalar theory of multiple scattering may be used instead, since polarization effects can then be neglected (Paganin, 2006). Since backscattering is also negligible, the forward-scattering recursive multislice scheme may then be used (Hare & Morrison, 1994; Thibault *et al.*, 2006). Backscattering at normal incidence is proportional to $R = (1 - n)/(1 + n)$, where n is the refractive index, and is therefore small for soft X-ray energies. It is also limited by the scattering kinematics. The theoretical treatment then becomes similar (but not identical) to that used for multiply scattered high-energy electrons (HEED) in the same geometry (Bethe, 1929). An *ab initio* derivation of the multislice method for soft X-rays has been given by Thibault *et al.* (2006), in which they avoid the small-angle approximation commonly used for more efficient computation. (In the limit of sufficiently small slice thickness, the common parabolic approximation to the Ewald sphere produces convergence.) An additional factor $(1 - q^2/k^2)^{-1/2}$ (where $\mathbf{q}$ is the scattering vector and $\mathbf{k}$ is the X-ray wavevector) also occurs in Thibault's treatment, which can be neglected if significant scattering occurs only for scattering vectors much smaller than the incident wavevector, so that the resolution d is necessarily much larger than the wavelength. It is neglected in the following treatment.

Temperature effects ultimately impose a cutoff on scattering angle for coherent scattering.

Differences between the X-ray and electron diffraction cases can thus be summarized as follows. We define interaction constants $\sigma_e = \pi/\lambda E_o$ for electron diffraction (where E_o is the beam energy in volts) and $\sigma_X = r_e\lambda$ for soft X-ray diffraction (where r_e is the Thompson electron radius, 2.82×10^{-6} nm). Phase shifts due to transmission through a material with mean electrostatic potential V_o or mean charge density ρ_o are then $\sigma_e V_o t$ and $\sigma_X \rho_o t$, respectively, where t is the sample thickness. (The real part of the refractive index for X-rays is $\delta = \sigma_X \lambda \rho_o/2\pi$, where $\rho_o \simeq 333$ e nm^{-3} is a typical protein electron density, with mass density 1.35 g cm^{-3} and typical stoichiometry $H_{50}C_{30}N_9O_{10}S_1$. Values of mass density between 1.2 and 1.4 g cm^{-3} can be found in the literature.) More accurately, ρ_o should be replaced by complex ρ, which is related to the effective number of electrons participating in oscillator strengths for the nearby absorption edges, and this is the quantity that diffracts soft X-rays. The resulting 'object' for diffractive imaging may be treated as real only if there is no spatial variation in the imaginary part of the refractive index (Song *et al.*, 2008). Extinction distances for HEED $\xi_{\mathbf{q}} = \pi/\lambda V_{\mathbf{q}}$ are tens of nanometres, but microns for soft X-ray diffraction (SXRD). (Here $V_{\mathbf{q}}$ is a Fourier coefficient of electrostatic potential and $\xi_{\mathbf{q}}$ is a measure of the strength of multiple scattering, as discussed later in connection with Fig. 2.) The thickness of the sample $\Delta t = 1/(2\lambda\mathbf{q}^2)$ for which the phase shift due to Fresnel propagation becomes $\pi/2$ at resolution $d = 1/|\mathbf{q}|$ is 0.8 nm for HEED ($V_o = 2 \times 10^5$ eV, $d = 0.2$ nm) but 6.25 nm for SXRD ($\lambda = 2$ nm, $d = 5$ nm) if typical experimental conditions are used in each case. When applied to a sample of thickness Δt, this expression gives an estimate of the thickness and resolution limits of the projection approximation. However, the most important differences are the strength of the absorptive processes and the sign of the refractive phase shift. As shown in the next section, depending on the proximity to absorption edges, the photoelectric effect may completely dominate SXRD, whereas the imaginary part of the optical potential in HEED is often taken as about one tenth of the real part. For protein at 290 eV above the carbon K edge, the amplitude attenuation length is about 0.5 μm. For soft X-ray imaging, the energy range between the carbon and oxygen K edges is of particular interest (the 'water window'). Other differences between electron and X-ray multiple scattering include the much larger rocking-curve width $1/\xi_{\mathbf{q}}$ for HEED (which is a significant fraction of the Bragg angle, but seconds of arc for hard X-rays) and the much flatter Ewald sphere for HEED, resulting in a much larger domain of validity for the projection approximation. The relationship between the various approximations made in multiple-scattering theory are summarized in Goodman & Moodie (1974).

The consideration of signs in the multislice method requires some caution; the original Cowley–Moodie papers inadvertently provided a theory of positron diffraction because of a sign error, and a similar error appeared in Sturkey's theory (Saldin & Whelan, 1973). All signs are fixed by those in the wave equation if the time dependence is included, and this fixes signs in a plane-wave solution. Forms of both Maxwell's and Schrödinger's equations have appeared in different texts with different consistent signs, traceable ultimately to the Dirac equation for electrons. Since the refractive index for soft X-rays is less than unity (unlike that for high-energy electrons), the X-ray wavelength is increased in a medium. With wavevector $k_o = 1/\lambda$, an incident soft X-ray plane wave $\exp(-2\pi i k_o z)$ entering a medium of refractive index n becomes $\exp(-2\pi i k_o z)\exp(+2\pi i \delta k_o z)\exp(-2\pi\beta k_o z)$ in the medium, with δ positive. This fixes a positive sign in the multislice phase grating; the sign of the Fresnel propagator is fixed consistently by an 'empty lattice' approximation, where $\delta = 0$, resulting in the signs given in equations (8) and (9) below. [These are also the signs for positron diffraction and channelling (Howie, 1966).] For high-energy electrons, a negative sign is needed in the exponential in equation (8).

2. Does absorption kill off soft X-ray multiple elastic scattering?

The short linear intensity-absorption lengths for soft X-rays suggest that most X-rays may be annihilated by conversion to photoelectrons before the probability of a second elastic scattering event becomes appreciable. If this is so, multiple-scattering effects might be ignored. In this section we investigate this possibility for samples of protein.

Little can be said in general about the form of the distribution of multiple elastic scattering from a three-dimensional nonperiodic sample apart from statements about symmetry [despite our ability to simulate multiple scattering for particular cases (Saldin & Pendry, 1985)]. Unlike single scattering, which is subject to Friedel's law, three-dimensional multiple-scattering intensities reflect the true three-dimensional symmetry of the charge density. This provides a test for the presence of multiple scattering – for a sample charge density known *a priori* to lack inversion symmetry, the observation of symmetric diffracted intensities obeying Friedel's law indicates single-scattering conditions. For the simplified case where $\rho = \rho(x, y)$, the Fourier transform of the charge density in reciprocal space is confined to a plane through the origin, normal to the beam. For a nonperiodic sample, the use of a computational superlattice then allows extinction distances and excitation errors to be defined, using $\mathbf{q} \simeq \theta/\lambda = h/a$ (in one dimension) as a reciprocal-lattice vector for the superlattice of length a, where θ is the total scattering angle and h is an integer. (Note that $\mathbf{q}$ differs from that used elsewhere by 2π.) Extinction distances $\xi_{\mathbf{q}} = \pi/\sigma_X\rho_{\mathbf{q}}$ may be taken as a crude 'path length' for double elastic scattering and hence depend on scattering angle through the Fourier coefficients of the charge density $\rho_{\mathbf{q}}$. Since $\rho_{\mathbf{q}} < \rho_0 \simeq 333$ e nm^{-3} for proteins, we have $\xi_{\mathbf{q}} > 0.8$ μm at 290 eV, whereas the amplitude attenuation coefficient $2t_{abs} = 0.5$ μm at this energy, so we might expect comparable effects. In the simplest two-beam multiple-scattering theory, diffracted intensities oscillate in thickness with period $\xi_{\mathbf{q}}$ if the excitation error $S_{\mathbf{g}}$ (a measure of the Ewald-sphere curvature, where $\mathbf{g}$ is a reciprocal-lattice vector)

is zero. In this low-angle regime, $\xi_{\mathbf{q}}$ will therefore increase with angle as $\rho_{\mathbf{q}}$ falls off, and increase with increasing beam energy as σ_X decreases, as shown below in detailed calculations. In the many-beam case, the oscillation with thickness (or beam energy) is not strictly sinusoidal. Note that the phase-grating approximation [PGA, the exponential term in equation (8)], which is accurate at sufficiently low resolution for all thicknesses, predicts a sinusoidal variation of intensity with thickness (a different period for every point **r** in the sample). At high angles, excitation errors rapidly become very large for soft X-rays (unlike hard X-rays and electron diffraction), because the relatively small Ewald sphere of radius $1/\lambda$ is comparable to the resolution limit $|\mathbf{q}_{\max}|$. In this kinematic limit of dynamical theory, the effective extinction distance $\xi_{\mathbf{q}} = 1/S_{\mathbf{g}} << t_{\rm abs}$. This weak scattering, rapidly oscillating with thickness, is consistent with the kinematic single-scattering theory. Thus both the PGA and the single-scattering theory predict sinusoidal oscillations if $\rho = \rho(x, y)$.

The multislice method was used to simulate the thickness dependence of scattering from a 50/50 mixture of pure protein and water. A model charge density $\rho(x) = \rho_o t(x)$, representing three parallel strands of protein lying in a plane normal to the beam, was created as follows. Here $\rho_o = 2(\delta + i\beta)/(r_e\lambda^2)$ is the constant complex effective charge density, proportional to the effective number of electrons per atom contributing to the oscillator strengths. (This tends to the beam-energy-independent electrostatic charge density for harder X-rays if $\beta = 0$.) Thus all modulation of scattering arises from shape effects in the protein–water sample, which is taken to have uniform composition. Only the zero-order Fourier coefficient of the charge density is complex (leading to absorption). A projection of the charge density taken along the beam direction was taken to have the form $t(x) = \exp(-x^4/w)$ in the transverse direction x normal to the beam and the strands, as shown in Fig. 1. Here w is a width parameter, and the charge density is constant along the beam direction and along the strands. This produces a one-dimensional line of diffracted intensity normal to the strands, so that a one-dimensional multislice formalism was used. The superlattice dimension a = 1 μm was sampled at 2.5 nm intervals, each peak had a full-width of 25 nm and 199 sampling points were used in reciprocal space to $|\mathbf{q}_{\max}| = (199/1000)\ \mathrm{nm}^{-1}$. The resulting one-dimensional plots more clearly reveal imperfections in the inversion process than two-dimensional greyscale images, which are more difficult to quantify, and whose presentation depends on choice of brightness and contrast. However, we emphasize that extinction distances (and the severity of multiple scattering generally) will be different for two- or three-dimensional charge densities. The region of most severe absorption occurs just above the carbon K edge at 290 eV for proteins. There the linear intensity-attenuation distance for a typical protein ($H_{50}C_{30}N_9O_{10}S_1$) where λ = 4.27 nm is $t_{\rm abs}$ = 0.25 μm. [$I = I_o\exp(-\mu z)$ with $\mu = 4\pi\beta/\lambda = 1/t_{\rm abs}$, and $n = (1 - \delta_1) - i\beta_1$, where $\delta_1 = 0.0019$ and $\beta_1 = 0.00128$ at this energy, using a mass density of 1.35 g cm^{-3} for pure protein (CXRO, 2008).] Since typical cellular material may be at least 50% water (and contain lipids), we approximate the real part of the refractive index by the mean of the values for water and pure protein and set this mean equal to the maximum value of the model charge density shown in Fig. 1(*a*). The single-scattering diffraction pattern from this is shown in Fig. 1(*b*) based on equation (1). For water, $\delta_2 = 0.0022$ and $\beta_2 = 0.000157$ at this energy. The peak widths w were chosen to provide sufficient scattering at the resolution limit needed for these simulations, and were about five times the wavelength. The absorption coefficient used was also the mean of those of water and protein, so that the expression for the phase grating in one slice of the multislice formalism (thickness Δt) was $\exp[\pi i(\delta_1 + \delta_2)\Delta t/\lambda]\exp[-\pi(\beta_1 + \beta_2)\Delta t/\lambda]$. Half the phase grating is water and half protein, and the approximation is made that coherent scattering from this mixture is not greatly different from that from separated regions of each.

The severity of multiple scattering is most easily judged from the thickness dependence of the scattering, which, if not

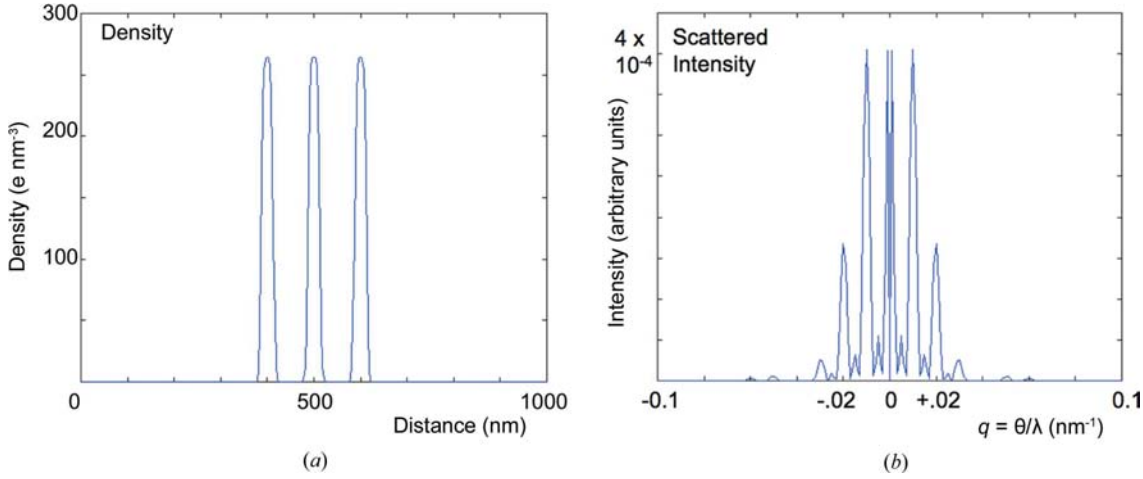

Figure 1
(*a*) The model electron density used throughout. 'Distance' is the real-space distance across the density peaks. The peak full-width is 25 nm. (*b*) The single-scattering far-field diffraction-pattern intensity produced by this electron density using 290 eV X-rays, just above the carbon K edge. θ is the scattering angle and q differs by 2π from that used elsewhere.

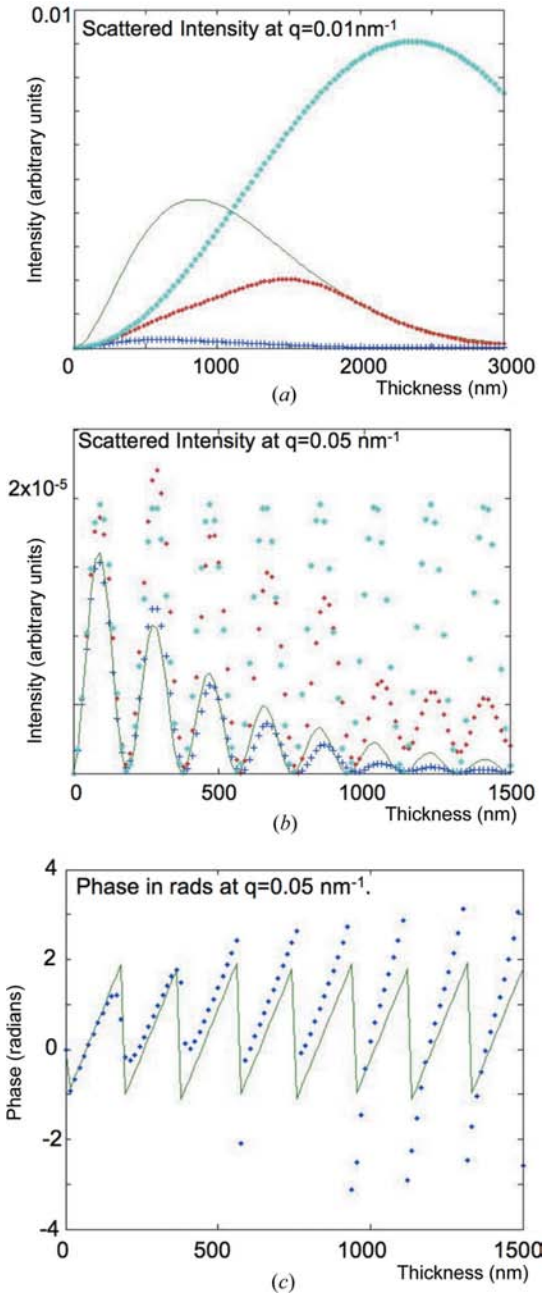

Figure 2
(*a*) The thickness dependence of soft X-ray multiple scattering at 290 eV for $q = \theta/\lambda = 0.01$ nm^{-1}. The top curve (star symbols) shows the single-scattered result (after division by 10) with the photoelectric absorption switched off. The continuous curve shows the single scattering with absorption. The curve shown with diamond symbols is the prediction of multiple-scattering theory without absorption. The lowest curve (plus signs) is multiple scattering with absorption. (*b*) Similar to (*a*), at a larger scattering angle with $q = 0.05$ nm^{-1} (20 nm spatial frequency), showing more rapid oscillation. The top curve (star symbols) shows the single-scattered result with the photoelectric absorption switched off. The continuous curve shows the single scattering with absorption. The curve shown with diamond symbols is the prediction of multiple-scattering theory without absorption. The final curve (plus signs) is multiple scattering with absorption. It is seen to follow the kinematic result with absorption reasonably well at lower thickness. (*c*) This figure compares the scattering phase plotted against thickness for single (continuous curve) and multiple (diamond symbols) scattering at $q = 0.05$ nm^{-1}. At low angles, where multiple scattering is stronger, phase distortions are more severe. The kinematic phase is given in equation (1).

angle-integrated, is initially proportional to the square of the thickness under single-scattering conditions. We show calculations at several energies: at 290 eV, where t_{abs} is a minimum, and at 500 eV, the highest energy in the water window commonly used with undulator insertion devices. (These results were also used for tests of the inversion algorithm.) Calculations are also given for 1.5 and 3 keV, well above the important biological inner-shell absorption edges. Fig. 2 shows multislice calculations for the scattering from these protein/water fibers as a function of their thickness (or, equivalently, of depth within the fiber) for two different scattering angles at a beam energy of 290 eV, where t_{abs} is a minimum. Fig. 2(*a*) shows curves for $|q| = \theta/\lambda = 1/d = 1/100$ nm^{-1} (low resolution) with and without the effects of the exponentially decaying photoelectric absorption envelope. Here θ is the total scattering angle. These two curves are compared with the predictions of single-scattering theory. In this figure we note the initial parabolic dependence of diffracted intensity on thickness, which is the signature of single scattering at the Bragg condition in crystals for data that are not angle-integrated. The single-scattering oscillation period (top curve) is seen to be much greater than the actual period when multiple scattering is included (next to lowest curve). However, the effect of absorption is dominant, causing the single (next to top curve) and multiple (lowest) scattering curves to differ mainly by a scale factor. In addition, the multiple-scattering curve falls off prematurely. Fig. 2(*b*) shows similar results at higher resolution (larger scattering angle) with $|q| = 1/20$ nm^{-1}. Again the curves that include absorption approximately follow each other (continuous line and plus signs), but now without much scaling. The net result will be an overemphasis on high spatial frequencies in the reconstructed images. At these higher angles (with larger 'excitation error') the single-scattering oscillation period $(0.5\lambda q^2)^{-1}$ is about equal to that of the multiple-scattering period, since this weaker scattering is less affected by multiple scattering.

Fig. 2(*c*) shows the variation of the phases with thickness, where the periodicities are now those of the curves in Fig. 2(*b*). The single-scattering intensities and phases are obtained from the expression

$$\psi(q) = (\sigma_X \rho_{\mathbf{q}} t)[\sin(\pi S_{\mathbf{q}} t)/\pi S_{\mathbf{q}} t] \exp(-i\pi S_{\mathbf{q}} t), \qquad (1)$$

where the phase factor (see Fig. 2*c*) depends on the choice of origin along z, and is here chosen at $z = 0$ to agree with the multislice boundary condition at the entrance face. $S_{\mathbf{q}}$ is defined in equation (4) below. Abrupt jumps in phase are due both to changes of sign in the sine function in this equation at each extinction period of the intensity (half that of the amplitude) and the method of plotting in $-\pi < \Theta < \pi$ (where Θ is the ordinate in Fig. 2*c*). At the lowest angles, the phases are controlled by the potential effect of the phase grating, rather than propagation, in accordance with the Glauber/Molier high-energy approximation for scattering (Ohmura, 1962). We note that the sign differences between electron, positron and soft X-ray multiple scattering have no effect on single scattering.

At higher beam energy, the intensity absorption distance has increased (to 0.7 μm for protein and 8 μm for water) as shown in Fig. 3 at 500 eV, just below the oxygen *K* edge. Here curves are again plotted for large and small scattering angles.

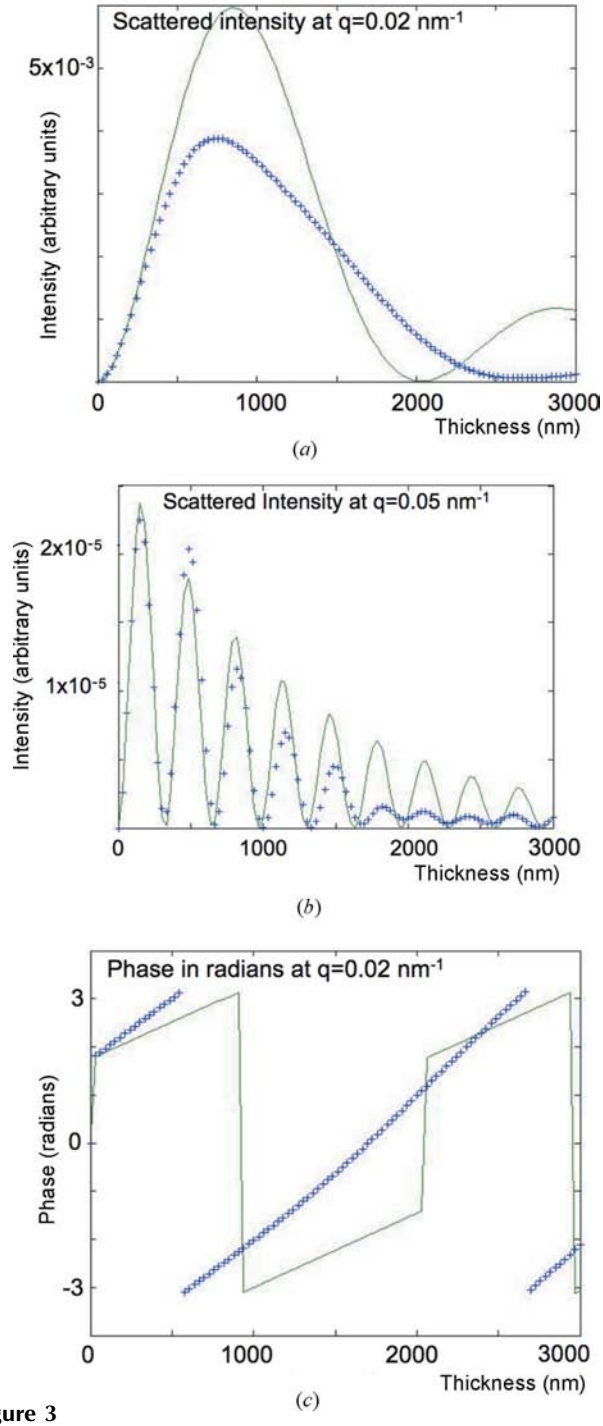

Figure 3
(*a*) The thickness dependence of the scattered intensity at 500 eV and q = 0.02 nm^{-1}, both curves with absorption. The continuous curve shows the single scattering, the crosses show the multiple scattering. (*b*) Similar to (*a*) for q = 0.05 nm^{-1}, showing more rapid oscillations. (*c*) Variation of phase (in radians) with thickness at q = 0.02 nm^{-1}. At higher angles, the agreement improves, as in Fig. 2. Note the second jump (phase reversal) in the continuous curve at the minimum of the single-scattering curve in Fig. 3(*a*).

For a thickness of less than half a micron, the effect of multiple scattering is now small at high and low angles. Fig. 3(*b*) shows similar behavior at a larger scattering angle, q = 0.05 nm^{-1}, with better agreement to higher thickness. The phase of the low-angle scattering also starts to deviate significantly from single-scattering predictions at about 0.5 μm thickness, as shown in Fig. 3(*c*). [The first jump in the curve is due to the method of display, the second is due to the sign change at every *intensity* period in the single-scattering theory, equation (1). This jump is not seen in the multiple-scattering curve.] These results are used for the inversion process described in the next section, which used thicknesses of 0.5 and 0.8 μm, where multiple-scattering effects start to affect phases and amplitudes. As for the lower-energy curves, both single- and multiple-scattering curves fall off exponentially at 500 eV, and increase with the square of thickness; however the premature fall-off of the multiple scattering at low angles is again seen, while better agreement is preserved at higher angles for this weaker scattering.

Figs. 4(*a*) and (*b*) show comparisons of single and multiple scattering with absorption at 1.5 and 3 keV, well above the important biological absorption edges. We see that the scattering at 3 keV remains kinematic to a thickness of at least 2 μm. Fig. 4(*c*) shows the phase variation, which remains relatively unaffected by multiple scattering to a thickness of about 2 μm, with much less error at higher angles. The longer extinction distance at 3 keV over 1.5 keV is noted. The use of these energies, although preserving single-scattering conditions to much larger thickness, suffers from the unfavorable λ^4 dependence of coherent scattered intensity when the effects of both the X-ray source and scatterer are considered (Howells *et al.*, 2008).

In summary, we find that whereas both single- and multiple-scattering curves commence with the correct parabolic thickness dependence, the low-angle multiple scattering shows a premature fall-off, not present at high angles, which will enhance high spatial frequencies in images. Phase distortions are also most severe at low angles. The net effect is that while absorption does greatly attenuate the effects of multiple scattering (for example, by eliminating the second oscillation in Fig. 3*a*), it must nevertheless be taken into account in order to obtain quantitative agreement for samples thicker than about half the extinction distance of the low-order scattering.

3. Scattering-matrix derivatives

We next establish that multiple scattering in SXRD is a function only of the product λt under reasonable approximations. We treat an isolated noncrystalline sample of thickness t within a much larger artificial periodic two-dimensional cubic unit cell of lateral dimension L, illuminated in transmission by a plane wave. Initially, the charge density within the cell is allowed to vary in an arbitrary manner along the beam path. Since the wavelength is much larger than interatomic spacings, modulation of the charge density ρ_o occurs only through shape effects, and the protein sample is assumed to have constant composition. The protein may be

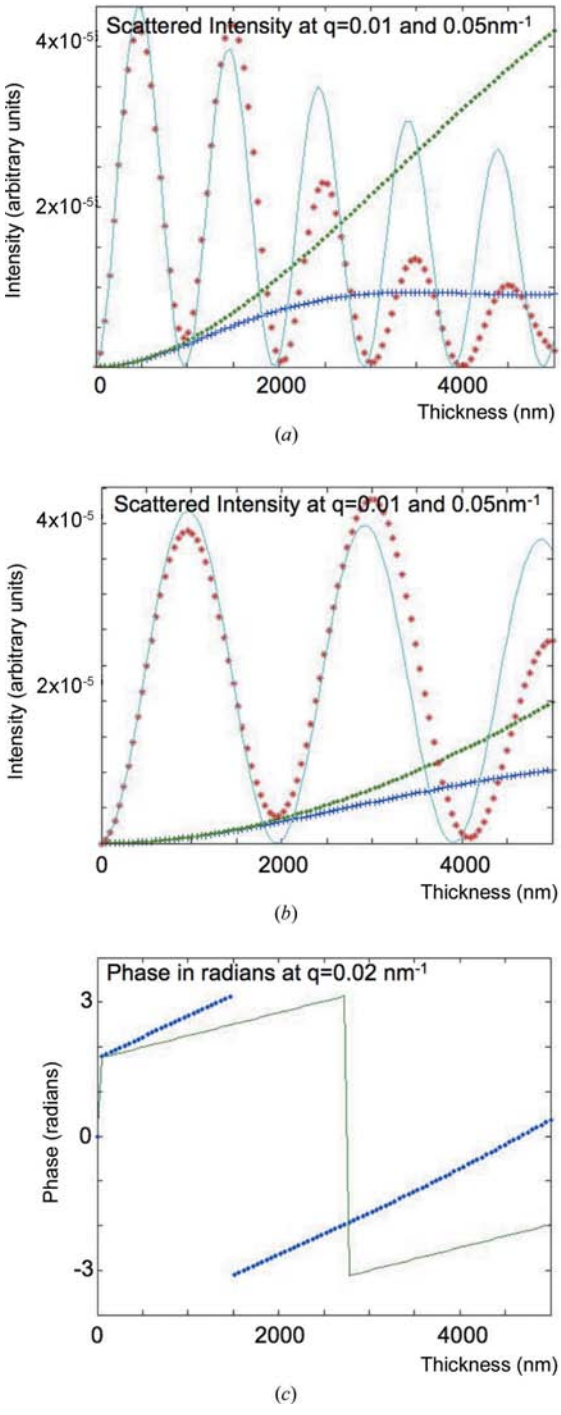

Figure 4
(*a*) The thickness dependence to 5 μm thickness of the scattering at 1.5 keV with absorption at high ($q = 0.05$ nm^{-1}, rapidly oscillating curves) and low angles ($q = 0.01$ nm^{-1}). The curves shown as diamonds and as a continuous line are for single scattering; the remaining are for multiple scattering. Good agreement is preserved to about 1 μm. The slowly varying curves have been divided by 10 000. (*b*) Similar to (*a*) at 3 keV ($\lambda = 0.413$ nm). Single scattering persists to 2 μm. Curves shown as diamonds and as a continuous line are for single scattering; the remaining are for multiple scattering. The intensity oscillates rapidly at high angles. (*c*) The variation of the phase at 1.5 keV at $q = 0.02$ nm^{-1}, comparing single (continuous curve) and multiple (diamond symbols) scattering. For weaker higher-angle scattering the agreement improves rapidly with angle: low-angle phases here agree to within half a radian at about 2 μm thickness.

embedded within an ice film, in which case only differences in refractive index are important (Kirz *et al.*, 1995), as discussed further below.

Following the Bloch-wave formulation of the scalar multiple-scattering theory extended to this case, where the sample is not periodic along the beam path, the Fourier coefficients of the dynamical wavefield at depth z within the sample can be formed into a column vector $\mathbf{u}$ (Tournarie, 1962), where

$$\mathrm{d}\mathbf{u}(\mathbf{z})/\mathrm{d}z = -2\pi i\mathbf{A}(z)\mathbf{u}(\mathbf{z}). \quad (2)$$

This equation also describes wave equations generally, including the Schrödinger equation if z is replaced by time and $\mathbf{A}$ is replaced by the Hamiltonian. We assume that the second-order derivative of $\mathbf{u}(z)$ in direction z is negligible (Koch & Spence, 2003). Then, for soft X-ray diffraction, the off-diagonal elements of $\mathbf{A}$ are proportional to the set of z-dependent Fourier coefficients $\mathrm{A}_{\mathbf{g}\text{-}\mathbf{h}}(z)$ of the two-dimensional charge density.

If $\mathbf{A}$ is independent of z for a charge density that depends only on the two-dimensional vector $\mathbf{r}$ normal to the beam, then the transform of the charge density is confined to a plane in reciprocal space through the origin and normal to the beam. Then the two-dimensional complex multiply scattered X-ray wavefield $\Psi(\mathbf{r})$ across the exit face of the sample is related to the far-field scattering $\varphi(\mathbf{q})$ by a Fourier transform. ($\mathbf{q}$ is the scattering vector which now terminates on the Ewald sphere.) The Fourier transform of the phased diffraction pattern no longer provides a faithful image of the charge density. We assume that, by iteration between the diffracted intensity distribution $\varphi\varphi^*$ and estimates of $\Psi(\mathbf{r})$ (which occupies a compact domain), the complex $\Psi(\mathbf{r})$ and hence $\varphi(\mathbf{q})$ can be found by using an algorithm such as *shrinkwrap* (Marchesini *et al.*, 2003) to solve the phase problem. By rotating the sample it is possible to arrange for $\mathbf{q}$ to explore all of reciprocal space within a sphere of radius $|\mathbf{q}_{\max}|$. For one orientation, the two-dimensional complex scattering distribution $\varphi(\mathbf{q})$ can be arranged to form the elements of a single vector $\mathbf{u}(z = t)$. An effective thickness may be defined by the absorption distance t_{abs}. The solution to equation (2) is then

$$\mathbf{u}(t) = \mathbf{S}\mathbf{u}_{\mathrm{o}} = \exp(2\pi i\mathbf{A}t)\mathbf{u}_{\mathrm{o}} \quad (3)$$

(Goodman & Moodie, 1974), where $\mathbf{u}_{\mathrm{o}}$ is a column vector containing Fourier coefficients of the incident coherent beam and $\mathbf{S}$ is unitary in the absence of spatially varying absorption. We have not assumed a flat Ewald sphere; however, the Fourier transform of the charge density is now confined to a plane through the origin of reciprocal space, normal to the beam.

Now the matrix $\mathbf{A}$ in this projection approximation has diagonal elements which are the excitation errors of the computational superlattice (Spence, 2003):

$$S_{\mathbf{q}} = |\mathbf{q}|^2\lambda/2, \quad (4)$$

which is positive for the soft X-ray case. The off-diagonal elements in $\mathbf{S}$ are the positive quantities $A_{\mathbf{q}} = r_{\mathrm{e}}\rho_{\mathbf{q}}\lambda/2\pi$, where $\rho_{\mathbf{q}}$ is a complex Fourier coefficient of the effective sample

charge density (number of electrons/volume). Then we can write

$$\mathbf{S} = \exp(2\pi i \mathbf{A}' \lambda t), \tag{5}$$

where $\mathbf{A}'$ is independent of λ and thickness t over any range of beam energy for which the effective number of electrons contributing to oscillator strengths is constant. Since ρ is taken to be spatially constant within a shape envelope, this requires in practice that absorption varies little over this beam-energy range. Any changes will then show up as scaling errors in the final result.

This establishes that multiple scattering for constant ρ depends only on the product of λ and t. The same result may be obtained from the Born-series expression of Moody (1972). Thus

$$\mathrm{d}\mathbf{S}/\mathrm{d}\lambda = (2\pi i \mathbf{A}' t)\mathbf{S},$$

allowing $\mathbf{A}$ to be found from the variation of $\mathbf{S}$ with λ if t is known. This expression yields both the ikonal approximation if $S_{\mathbf{q}} = 0$ and the Fresnel propagator if $\rho = 0$. While energy and momentum are strictly conserved only for elastic scattering involving transitions on the (curved) Ewald sphere, application of the uncertainty principle along the beam path indicates that scattering is allowed over a small range of $K_z = 1/t$ values which are inversely related to the sample thickness t.

4. Two-wavelength inversion using the multislice formulation

From equations (2) and (5), since $\mathbf{u}(t) = \mathbf{u}(\mathbf{q}, t, \lambda)$ contains the Fourier coefficients of $\Psi(r, t, \lambda)$, we see that

$$\Psi(\mathbf{r}, t, \lambda) = \Psi(\mathbf{r}, \lambda t). \tag{6}$$

Let $c = \lambda t$. Then the dynamical solution will be unchanged if $\delta c = 0$ or $t\delta\lambda = -\lambda\delta t$, so that a change $\delta\lambda$ in wavelength is equivalent to a change $-\delta t$ in thickness. Hence

$$\begin{aligned}\Delta\Psi(r) &= \Psi(\lambda_1, t + \Delta t) - \Psi(\lambda_1, t)\\ &= \Psi(\lambda_1, t + \lambda_1 \Delta t) - \Psi(\lambda_1, t)\\ &= \Psi[(\lambda_1 - \Delta\lambda), t] - \Psi(\lambda_1, t).\end{aligned}$$

The use of a difference in wavelength is thus equivalent to small change in thickness, and the difference $\Delta\Psi$ can provide a single-scattering wavefunction.

In summary, with beam energy E, we therefore have

$$\Delta t/t = -\Delta\lambda/\lambda = \Delta E/E. \tag{7}$$

The multislice formulation of the multiple-scattering problem produces the Born series in the limit of vanishing slice thickness and increasing slice number, and so is consistent with the results of §3. We now use this multislice formulation to obtain expressions for the two-dimensional complex real-space wavefield at two adjacent wavelengths and constant thickness. The multislice iteration is

$$\Psi_2(r, t + \Delta t, \lambda) = \Psi_1(r, t, \lambda) \exp(r_e |\rho(r)| \Delta t \lambda) * P(r, \lambda \Delta t), \tag{8}$$

where $\mathbf{r}$ is a two-dimensional vector normal to the beam, $*$ denotes convolution and the propagator P is

$$P(r) = \exp(-i\pi |\mathbf{r}|^2 / \lambda \Delta t)$$

with Fourier transform

$$P(q) = \exp(2\pi i S_{\mathbf{q}} \Delta t) = \exp(\pi i \Delta t \lambda |\mathbf{q}|^2), \tag{9}$$

where $S_{\mathbf{q}}$ is positive. Then

$$\begin{aligned}\Psi_2(r, t, \lambda + \Delta\lambda) &= \Psi_2[r, \lambda t(1 + \Delta t/t)]\\ &= \Psi_1(r, t, \lambda) \exp[r_e \rho(r) t \Delta\lambda] * P(r, t\Delta\lambda).\end{aligned} \tag{10}$$

This gives the relationship between multiply scattered wavefields at slightly different beam energies for a sample thickness t. We can therefore obtain the charge density from the difference or division of complex images recorded at two adjacent wavelengths. We have

$$\frac{\Psi_2(r, t, \lambda + \Delta\lambda)}{\Psi_1(r, t, \lambda)} = \exp[r_e \rho(r) t \Delta\lambda] * P(r, t\Delta\lambda). \tag{11}$$

This expression may be solved for $\rho(r)$ by Fourier deconvolution of the propagator, which is achieved by multiplying the Fourier transform of equation (11) by the conjugate of equation (9). Where $\Delta\lambda$ is small, the first-order expansion of the exponential then provides the quantity $\rho(r)$ if t and $\Delta\lambda$ are known. The absolute scaling of the charge density then requires a knowledge of sample thickness, but this is often not needed or may be obtained from a reference atom. A Weiner filter may be used to control the magnitude of the result if the denominator becomes zero in the presence of noise. The choice of $\Delta\lambda$ should introduce a significant phase shift, of say $\pi/8$, within the weak-phase-object approximation, so that

$$\Delta\lambda = \pi/(8 r_e \rho t) \tag{12}$$

or 0.2 nm for t = 2000 nm. The method assumes that the change in absorption across this wavelength range is negligible (or accurately known); the wavelength range should be chosen accordingly. The method requires an approximate knowledge of thickness if quantitative results are expected. Diffraction patterns recorded at slightly different energies will vary in size, so that reference periodicities may be needed for rescaling.

5. Computational trials

Simulated inversions have been demonstrated based on equations (9) and (11) for several cases. The thickness region in which dynamical inversion is possible must be greater than that which produces single scattering, and less than that for which all photons are absorbed by the photoelectric effect. From Fig. 2, we see that this window depends on the beam energy and the scattering angle. We also prefer small known variations in absorption over the wavelengths chosen. Study of the linear attenuation distance for a typical protein suggests a best energy of about 500 eV, between the carbon and oxygen K edges, where λ = 2.478 nm and $I = I_o \exp(-\mu z)$ [where μ =

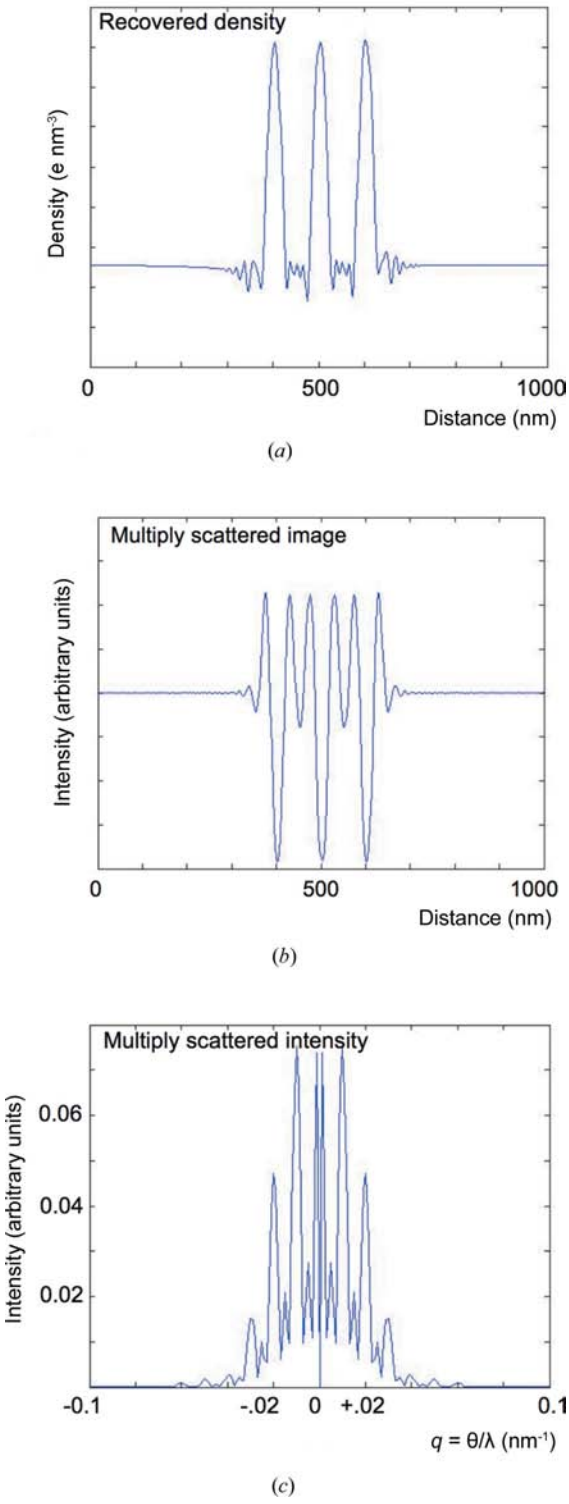

Figure 5
(*a*) The charge density recovered by this inversion algorithm using diffraction-pattern intensities simulated for 500 and 450 eV, for comparison with Fig. 1(*a*). The ordinal increment is 50 e nm^{-3}, as for Fig. 1(*a*). The thickness is 0.5 µm, at the onset of multiple-scattering perturbations, particularly in phase at low angles. (*b*) The multiply scattered image intensity at 500 eV, showing severe distortion. This is the Fourier transform of the complex pattern shown in (*c*). (*c*) Diffraction-pattern intensity at 500 eV used to obtain (*a*), showing strong multiple-scattering perturbations when compared to Fig. 1(*b*).

$4\pi\beta z/\lambda = z/t_{\rm abs}$, $n = (1 - \delta) - i\beta$, $\delta = 0.001$, $\beta = 0.000295$ and $t_{\rm abs}$ = 0.669 µm for $H_{50}C_{30}N_9O_{10}S_1$ with a mass density of 1.35 g cm^{-3} for pure protein at this energy (CXRO, 2008)]. Since typical cellular material may be at least 50% water (and contain lipids) we approximate the real part of the refractive index by the mean of the values for water and pure protein and set this mean equal to the average value of the model charge density shown in Fig. 1. For water, $\delta = 0.00062$ and $\beta = 2.396 \times 10^{-5}$ at this energy.

Conditions for convergence of the multislice formulation have been discussed extensively in the literature [see especially Anstis (1977)] – the weak-phase-object approximation is not made for each slice and the propagator phase shift may exceed $\pi/2$; however, a reduction in slice thickness should not affect the intensity predictions. The two-wavelength method also assumes separability of Fresnel and potential-energy effects for small wavelength changes, so that the wavelength difference chosen must be one for which a multislice method based on equations (10) and (7) would converge. The wavelength change must also fall within the weak-phase-object approximation.

Fig. 5(*a*) shows the charge density recovered using equation (11) from a thickness of 0.5 µm, using beam energies around 500 eV, which is seen from Fig. 3 to fall at the onset of the multiple-scattering region, especially for low-order phase distortions. Complex diffraction patterns were simulated at 500 and 450 eV, corresponding through equation (6) to a 10% change in beam energy or sample thickness. (This is considerably greater than the degree of monochromaticity commonly used in SXRD.) The charge-density profile shown in Fig. 1(*a*) has been recovered with reasonable accuracy. Fig. 5(*b*) shows the Fourier transform of a single 500 eV diffraction pattern, being the exit-face wavefield or multiple-scattering image, demonstrating severe image distortion. Fig. 5(*c*) shows the diffraction-pattern intensity.

Fig. 6 shows the same charge density recovered from a larger thickness of 0.8 µm, well into the multiple-scattering

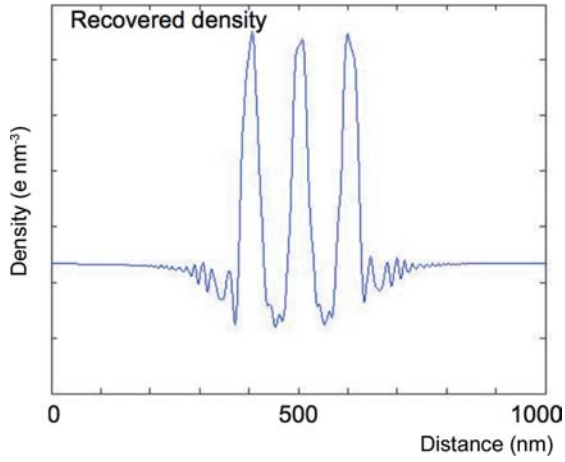

Figure 6
(*a*) Charge density recovered by the inversion algorithm using diffraction patterns simulated for 500 and 480 eV, for comparison with Fig. 1(*a*). The ordinal increment is 50 e nm^{-3}, as for Figs. 1(*a*) and 5(*a*). Thickness 0.8 µm.

region, using beam energies of 500 and 480 eV. The inversion is found to give results which are almost independent of thickness. A known object, such as a gold nanoball, might be used to optimize the choice of deconvolution focus $\Delta\lambda$ in equation (11).

6. Dynamical tomography

We now consider again the case where $\rho(\mathbf{r}, z)$ is an unknown function of z. Leaving aside optical sectioning techniques that assume single scattering, two approaches to three-dimensional reconstruction of ρ are common. The first aims to assemble the complete three-dimensional Fourier transform of ρ from complex scattered amplitudes restricted by scattering kinematics to the Ewald sphere, which is then swept through most of reciprocal space (or equivalently, by rotating the sample about an axis normal to the beam). The second, less efficient, method reconstructs real-space image projections for each orientation of the sample, then assembles these into a three-dimensional charge density by methods such as filtered back-projection. The question arises as to whether either can be adapted to these results.

The complex Fourier transform of the charge density ρ on the zero-order Laue zone corresponds to a projection of ρ. If this can be recovered for every orientation of the sample, a three-dimensional reconstruction of the charge density can be obtained. If $\rho = \rho(\mathbf{r}, z)$, then the three-dimensional multislice iteration becomes

$$\Psi_{n+1}(r, t + \Delta t, \lambda) = \Psi_n(r, t, \lambda) \exp[r_e \rho_p^n(r)\lambda] * P(r),$$

which exactly solves Maxwell's equations in the limit as the slice thickness is taken to zero for soft X-rays (Paganin, 2006; Thibault *et al.*, 2006). Here

$$\rho_p^n(r) = \int_0^{\Delta t} \rho^n(r, z)\, \mathrm{d}z$$

is the charge density in the nth slice. This formulation, in which every slice is different, takes correct account of multiple scattering along the beam path. Reciprocal space is sampled at intervals $1/\Delta t$ along the z direction. Since $\rho_p^n(r)$ is not in general proportional to Δt, the solution is no longer a function of the product λt, and changes in wavelength no longer mimic those of thickness as required for equation (11) to hold. The ability to vary λ no longer provides a method for extracting $\rho(\mathbf{r}, z)$, except in the trivial case where λ is so small that the scattering is kinematic, or for the case of a sample such as a crystal, periodic along z, in which every slice can be chosen to be the same.

We note that the PGA [the exponential term in equation (8)], which is accurate at sufficiently low resolution for all thicknesses, predicts a sinusoidal variation of intensity with thickness (a different period for every point r in the sample). This approximation, which holds if $\pi S_{\mathbf{q}} t < \pi/2$ in equation (4), also allows two-wavelength inversion for tomography. By restricting both the resolution and the sample thickness, it may be possible to find conditions in which the PGA holds. Then the inversion scheme above may be combined with the second back-projection form of tomography at low resolution. The refinement of high-resolution detail could then be attempted by matching forward-multiple-scattering calculations to the images. This approach ignores the redistribution to high angles of low-angle scattering, which must strictly be included in any inversion scheme. Alternatively, a formulation of the problem in which lateral scattering is treated dynamically but scattering along the beam path is treated kinematically may be useful. Refractive-index matching, discussed below, may also assist the tomography problem.

7. Conclusions

On the question of whether absorption eliminates multiple scattering, we find that it has the effect of greatly attenuating multiple-scattering effects, but that a premature fall-off in intensity with thickness at low angles (not present at high angles) will lead to the enhancement of high spatial frequencies in diffractive images. We also find phase distortions in low-angle scattering for thicknesses greater than the low-angle extinction distance. More rapid oscillations of the soft X-ray case compared to electrons might be expected, due to the fact that the phase-grating phase shift is in the same direction as the propagator (in real space). Other factors, however, such as the weaker interaction and more rapid increase of excitation errors with angle, mitigate and modify this effect, while the dominance of photoelectric absorption suppresses thickness oscillations (producing a scaled version of the single-scattering form) which would otherwise occur at low angles.

This paper has also attempted to provide a first step in approaching the hitherto intractable problem of dynamical inversion for many-beam cases. It recovers the same charge density from all thicknesses of sample despite multiple scattering, but is limited to objects with a two-dimensional shape envelope. (It fails, for example, for a spherical cell of constant charge density.) For three-dimensional scattering distributions the multiple scattering will be weaker, since it is no longer concentrated into a line and hence the absorptive effect will be greater in reducing multiple-scattering artifacts. To extend this two-wavelength approach, we may consider several possibilities as follows. Apart from the few-beam dynamical phasing methods used in protein crystallography, previous work has been limited to simulations. The most promising approaches have been:

(1) the method of Allen *et al.* (2000), which provides an exact non-iterative recovery of **A** [equation (5)] from a knowledge of all of complex **S**;

(2) the two-thickness method of Allen *et al.* (2001), closely related to the approach of this paper;

(3) the dynamical ptychography method of Spence (1998); and

(4) the hybrid input–output method, including multiple-scattering effects (Spence *et al.*, 1999). That approach, which iterates between the multiple-scattering amplitudes and the charge density, utilizes the fact that multiple scattering, by allowing interference between scattering in different direc-

tions, 'solves' the phase problem by making multiply scattered intensities sensitive to the phases of the Fourier coefficients of the charge density (the structure factors).

Beyond these approaches for the treatment of scattering along the beam direction, approximations exist in which this can be treated kinematically, with multiple scattering allowed only laterally. It remains to be determined whether such an approximation would permit inversion at two wavelengths to a three-dimensional charge density from tomographic data. Finally, we note that this paper treats an isolated object, which may be required to enable iterative phasing [but see Rodenburg (2008)]. For the case of a cell lying entirely within a parallel-sided slab of ice (as in cryo-electron microscopy), one has an entirely different situation in which only the difference between the refractive index of the ice and that of the protein are important (Kirz *et al.*, 1995). As in small-angle X-ray scattering studies, the refractive properties of the ice might then be modified to be close to that of protein, and so minimize multiple scattering. For a cell, these modifications must not affect the environmentally sensitive lipid structure of the cell membrane. If the protein is treated as a homogeneous unresolved mass of constant composition, then only the zero-order Fourier coefficient of the charge density is complex (leading to absorption) and the real-object approximation may be made if experimental diffraction patterns show Friedel symmetry. In this case the three-dimensional shape envelope may be determined. In practice, soft X-ray patterns from whole cells may not show Friedel symmetry (Shapiro *et al.*, 2005) and give evidence of multiple scattering. At higher resolution, where spatial variations of, for example, carbon-atom concentration are resolved (present in protein but not water), the phasing of the resulting complex object will create significant difficulties. These are addressed with varying degrees of success by the four phasing methods mentioned in §1 and would allow tomographic reconstruction of internal detail.

We note that the in-focus reconstruction of an image in the single-scattering thickness region will show negligible contrast if the zero-order beam is included, since this is a bright-field phase-contrast image. Access to the complex image amplitudes in computer-based diffractive imaging, like holography, allows the formation of a large variety of different types of images (dark field, bright field *etc*., at any focus setting) not possible using conventional lens-based imaging, where intensities are detected directly. These many forms of image may be obtained by modifying the deconvolution propagator term in equation (11) during reconstruction.

Equation (6) also holds true for nonrelativistic electron diffraction in the axial orientation, thus allowing this method to be applied in principle to low-energy transmission electron diffraction. However, the inverse square-root dependence of the de Broglie wavelength on the beam energy, the requirement for low nonrelativistic energies in the transmission geometry (with very limited penetration) and the difficult quantification of continuous electron scattering from isolated nonperiodic objects in the presence of substrate scattering (Zuo *et al.*, 2003) all make electron experiments using two wavelengths extremely difficult.

This work was supported by NSF award IDBR0555845. I am grateful to Professor P. Rez for useful discussions.

References

Allen, L. J., Faulkner, H. M. L. & Leeb, H. (2000). *Acta Cryst.* A**56**, 119–126.

Allen, L. J., Koch, C., Oxley, M. P. & Spence, J. C. H. (2001). *Acta Cryst.* A**57**, 473–474.

Anstis, G. R. (1977). *Acta Cryst.* A**33**, 844–846.

Bethe, H. (1929). *Ann Phys.* **87**, 55–128.

Chapman, H., Barty, A., Marchesini, S., Noy, A., Cui, C., Howells, M., Rosen, R., He, H., Spence, J. C. H., Weierstall, U., Beetz, T., Shapiro, D. & Jacobsen, C. (2006). *J. Opt. Soc. Am.* **23**, 1179–1189.

Cowley, J. M. (1995). *Diffraction Physics*, 3rd ed. New York: North Holland.

CXRO (2008). *Center for X-ray Optics*, http://www-cxro.lbl.gov/.

Goodman, P. & Moodie, A. F. (1974). *Acta Cryst.* A**30**, 280–290.

Hare, A. R. & Morrison, G. R. (1994). *J. Mod. Optics*, **41**, 31–43.

Hirsch, P., Howie, A., Nicholson, R. A., Pashley, D. & Whelan, M. (1977). *Electron Microscopy of Thin Crystals*. New York: Krieger.

Howells, M., Beetz, T., Chapman, H., Cui, C., Holton, J., Jacobsen, C., Kirz, J., Lima, E., Marchesini, S., Miao, H., Sayre, D., Shapiro, D. & Spence, J. C. H. (2008). *J. Electron Spectrosc. Relat. Phenom.* In the press.

Howie, A. (1966). *Philos. Mag.* **4**, 223–229.

James, R. W. (1965). *The Optical Principles of the Diffraction of X-rays*. Ithaca: Cornell University Press.

Kirz, J., Jacobsen, C. & Howells, M. (1995). *Quart. Rev. Biophys.* **28**, 33–130.

Koch, C. T. & Spence, J. C. H. (2003). *J. Phys. A*, **36**, 803–816.

Marchesini, S., He, H., Chapman, H. N., Hau-Riege, S. P., Howells, M., Noy, M., Weierstall, U. & Spence, J. C. H. (2003). *Phys. Rev. B*, **68**, 140101.

Miao, J., Charalambous, C., Kirz, J. & Sayre, D. (1999). *Nature (London)*, **400**, 342–343.

Moody, A. F. (1968). Personal communication.

Moody, A. F. (1972). *Z. Naturforsch.* **27a**, 437–444.

Ohmura, T. (1962). *Quantum Theory of Scattering*. New York: Prentice-Hall.

Paganin, D. (2006). *Coherent X-ray Optics*. New York: Oxford University Press.

Pinsker, Z. G. (1978). *Dynamical Scattering of X-rays in Crystals*. New York: Springer.

Rodenburg, J. M. (2008). *Ptychography and related diffractive imaging methods. Adv. Imag. Electron Phys.* In the press.

Saldin, D. & Pendry, J. (1985). *Surf. Sci.* **162**, 941–944.

Saldin, D. & Whelan, M. J. (1973). *J. Phys. C*, **6**, L215–L218.

Shapiro, D., Thibault, P., Beetz, T., Elser, V., Howells, M., Jacobsen, C., Kirz, J., Lima, E., Miao, H., Neiman, A. & Sayre, D. (2005). *Proc. Natl Acad. Sci. USA*, **102**, 15343–15346.

Song, C. R., Bergstrom, D. R., Johnson, H., Jiang, D., Paterson, M., de Jonge, I., McNulty, J., Lee, K. & Wang, J. M. (2008). *Phys. Rev. Lett.* **100**, 026604.

Spence, J. C. H. (1998). *Acta Cryst.* A**54**, 7–18.

Spence, J. C. H. (2003). *High Resolution Electron Microscopy*, 3rd ed. Oxford University Press.

Spence, J. C. H. (2007). *Diffractive (Lensless) Imaging.* In *Science of Microscopy*, Vol. 2, edited by P. Hawkes & J. C. H. Spence, pp. 1196–1227. New York: Springer.

Spence, J. C. H., Calef, B. & Zuo, J. M. (1999). *Acta Cryst.* A**55**, 112–118.

Sturkey, L. (1962). *Proc. Phys. Soc.* **80**, 321–354.

Thibault, P., Elser, V., Jacobsen, C., Shapiro, D. & Sayre, D. (2006). *Acta Cryst.* A**62**, 248–261.

Tournarie, M. (1962). *J. Phys Soc. Jpn*, **17**, 98–100.

Zuo, J. M., Vartanyants, I. A., Gao, M., Zhang, M. & Nagahara, L. A. (2003). *Science*, **300**, 1419–1421.